applied optics

Simulation and calibration of a compact millimeter-wavelength Fourier transform spectrometer

Mira Liu,[1,2] Zhaodi Pan,[1,2] Ritoban Basu Thakur,[3] and Stephan S. Meyer[1,2,4,5,*]

[1]Kavli Institute for Cosmological Physics, University of Chicago, 5640 S. Ellis Ave., Chicago, Illinois 60637, USA
[2]Department of Physics, University of Chicago, 5640 S. Ellis Ave., Chicago, Illinois 60637, USA
[3]California Institute of Technology, MC 249-17, Pasadena, California 91125, USA
[4]Department of Astronomy and Astrophysics, University of Chicago, 5640 S. Ellis Ave., Chicago, Illinois 60637, USA
[5]Enrico Fermi Institute, University of Chicago, 5640 S. Ellis Ave., Chicago, Illinois 60637, USA
*Corresponding author: meyer@uchicago.edu

Received 23 June 2020; revised 20 July 2020; accepted 22 July 2020; posted 24 July 2020 (Doc. ID 397312); published 1 September 2020

This paper presents the simulation and calibration of a Fourier transform spectrometer (FTS) developed to measure the spectrum of radiation sources between 50 GHz and 330 GHz, such as the cosmic microwave background. The recorded signal is modified from the ideal by properties of the interferometer and the detection system. We have developed a ray-trace-based simulation with which we can model these effects. The model can be verified with measurements and used to understand the instrument's systematic effects and to design new optimized configurations. The optimization comprises parameters of the design, such as large étendu, maximal spectral resolution, compact size, operational simplicity, and light weight, that conflict and need to be balanced. The numerical simulation consists of two parts: time-stream signal analysis and a ray-trace-based simulation that includes polarization and path length calculations and can account for the effects of beam loss and change of focus as the delay-generating mirror travels on its path. The simulation can study the coherence level and frequency resolution of the FTS instrument. While not exercised in this study, the simulation also can be used to study the effect of mirror figure and polarizer non-idealities, walk-off rays in the beam due to the large étendu, as well as misalignment of optical elements. We then present the comparison between simulations of a spectrally unresolved source and measurements by the FTS. © 2020 Optical Society of America

https://doi.org/10.1364/AO.397312

1. INTRODUCTION

A Fourier transform spectrometer (FTS) similar to a design developed for a satellite mission, PIXIE [1], has been constructed to be used for measurements of the spectral response of the kilo-pixel radiometer on the South Pole Telescope [2,3]. The essential features of the FTS are light weight, compact size, and maximal spectral resolution. The system uses a series of confocal mirrors machined into the exterior of the structure to fold the light path. The folded path enables a system with simple operation, high throughput, and compact size.

The FTS was subjected to an extensive set of calibration tests consisting of varying the path length motion of the mirror, changing mirror speed, and using a variety of sources including thermal sources, band defining filters, as well as narrowband coherent sources at 90, 144, and 295 GHz [4]. The test data are compared to the numerical simulation, which can be used to explore the properties of the FTS that cannot be easily be disentangled but are essential for global optimization. Additionally, the effect of non-idealities, such as mirror tilts, imperfect polarizers, and scattering, can be studied with ray-tracing simulations. The simulation can be used to predict FTS properties such as optical efficiency, actual throughput, frequency accuracy, and frequency resolution.

2. INSTRUMENT

A. Instrument Description

The FTS is designed to measure electromagnetic spectra in the frequency range of 50 GHz to 330 GHz. The radiation propagates from the source through a series of mirrors and wire-grid polarizers to an output mirror, as shown in Fig. 1 [4,5]. The configuration is a Mach–Zehnder interferometer [6–8] with the two central polarizers (P2 and P3) acting as beam splitters, and the difference in the length of the two paths between them (the optical delay) is determined by the position of the center flat double-sided moving mirror. The detector at the output focal

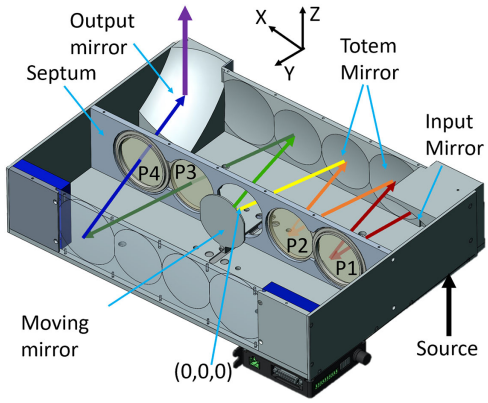


Fig. 1. Shown is a rendering of a CAD model of the FTS with the two nearest walls, the central polarizer support wall (marked as "septum"), and the top shown as transparent. The source is on the bottom right shown as a black arrow and illuminating an off-axis elliptical mirror, which launches a 70 mm diameter beam into a system of polarizers at the center and reimaging mirrors machined into the outer walls of the box. The polarizers are labeled P1 through P4. A moving flat mirror between P2 and P3 introduces the delay of the interferometer. The coordinate axes are those used throughout this paper, and the origin is at the center of the moving mirror in its zero path position labeled as (0,0,0). The colored arrows illustrate one of the possible optical paths, starting with the lower right black arrow input beam. In this implementation of the device, an ambient temperature absorber, shown here in blue, covers the second import port at the lower left. The output is sent out of the box by a second off-axis ellipse and forms a focus 38 mm above the top of the box (violet arrow). The corresponding second output is on the left and also has an ambient temperature absorber. For the first two polarizers, only the reflected path is shown (red and orange beams). For the second two polarizers, only the transmitted path is shown (dark green and blue beams). The moving mirror (shown at maximum $-y$ position) reflects the yellow beam to the light green beam.

plane measures the power in the recombined radiation from the two light paths. The output power as a function of optical delay is the Fourier transform of the input source spectrum [9]. Figure 1 shows a rendering of a computer-aided design (CAD) model of the FTS and one possible radiation transfer path through the FTS.

In Fig. 1, polarizer P1 is oriented with the wires at 45 deg to the z axis, and the light transmitted by P1 is split evenly by the following beam splitter (P2) whose wires are oriented along the z axis. Polarizer P3 is oriented along the x axis, so light transmitted by P2 is reflected by P3, and the light reflected from P2 is transmitted by P3. Since the mirror position changes the differential path length of the two beams, the light leaving P3 is the sum of two orthogonal linear polarized beams resulting in a modulated elliptical polarization. Polarizer P4 then converts that elliptically polarized input light into linearly polarized light with modulated amplitude at the output. Radiation reflected by P1 undergoes the same modulation, but with polarizations reversed and transmission and reflection exchanged. This combination of polarizers can modulate both polarizations in the input radiation at a 100% level, with no losses in principle.

Each mirror machined into the box sidewall is a section of an ellipse of rotation, its two foci at the center of the previous and subsequent mirrors. The set of four mirrors on each side form

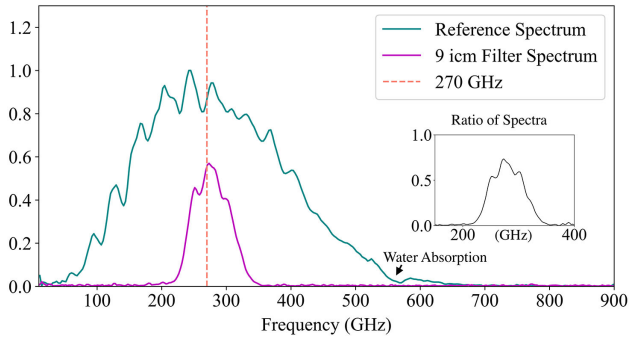


Fig. 2. Shown is an example spectrum measured by the FTS with a 1300 K thermal source coupled to the input. The detector has a low-pass filter (25 mm of Fluorogold [10]), which cuts off higher-frequency components. The green curve does not have further filters in the optical path, while the purple curve is with a bandpass filter centered at 270 GHz. The spectrum without the filter agrees with our expectation, with the water absorption line at 550 GHz marked. [5]. The spectrum with the filter peaks at 270 GHz as expected. The inset graph shows the ratio of the two spectra and is a measurement of the filter transmission. The figure demonstrates the broadband performance of the FTS. The green spectrum is the Fourier transform of the interferogram shown in Fig. 5.

a series of reimaging optics called totem mirrors that control the beam geometry. The output mirror is also elliptical, with one focus on the previous mirror and the other focus at the output focal plane. The input mirror is similar. The detector and source planes are located 38 mm above or below the box. A more detailed review of the FTS structure and the function of each element is given in Ref. [4]. In operation, the instrument typically has a thermal source at the input and a receiver under test with its input confocal with the detector plane of the FTS.

In operation, the mirror scans from one side of the septum to the other, and the power output is detected and recorded, giving an interferogram whose Fourier transform is the spectrum of the input source. Figure 2 shows the measured spectra of a 1300 K blackbody source and the same blackbody with a bandpass filter.

3. RAY-TRACING SIMULATION

A. Simulation Overview

A ray-tracing simulation code was developed to study the radiation transfer and interference efficiency (contrast) through the geometry of the FTS as a function of delay. These properties affect the efficiency and resolution of the instrument but are difficult to evaluate analytically. Each simulated ray starts at the source plane with a random position and angle following the source beam profile and angle probability. The rays are propagated through the system with calculations for the interactions with the optical elements. The current iteration of the simulation assumes that the optical surfaces follow the ideal design shape, are perfectly smooth, and that the polarizer properties are ideal. Each ray is propagated with information about the polarization and phase as it travels through the instrument. With this, the simulation can also model the FTS' limitations, such as

- total throughput,

- detector and source size and geometry,
- scatter from mirrors or polarizers,
- beam loss by occlusion or rays missing mirrors,
- decoherence due to path differences of high-angle rays,
- decoherence due to spatial separation of rays,
- non-ideal polarizer properties,
- mirror shape variations either from non-ideal manufacture or for optimization purposes.

The pattern of rays at the detector varies as the mirror moves. In our simulation, we assume a small, single-mode detector with a perfect lens at the output plane of the instrument. Any single-mode detector having a horn with a known input phase shape at the input can also be modeled since the phase of the arriving ray is calculated. However, this numerical simulation does not simulate diffraction at intermediate apertures and cannot model the acceptance of a multimode detector due to the ray-tracing nature of the simulation. This means that the effect of spatial separation is not reflected in the simulated power and interferograms. But the amount of spatial separation can be approximated by geometric ray tracing and is presented in Section 4.B.

B. Simulation of Propagation

Each ray starts with an initial linear polarization. From that, the phase, position, direction, and intensity of all rays are tracked to one of the output ports. A ray is represented by $R \equiv [\theta, E_0^2, p, \vec{v}, D]$. θ is the linear polarization angle, and E_0^2 is proportional to the intensity of the ray I ($E_0^2 \propto I$). $p = [x, y, z]$ is the launch position, $\vec{v} = [v_x, v_y, v_z]$ is the unit vector of direction, and D is the total distance traveled from the source. A ray launched at the source is given a polarization angle, unity intensity, a position, a launch vector, and an initial travel distance of zero. Rays interact with the FTS optics by reflections from mirrors and reflections and transmissions from polarizers. When a ray R interacts with an optical component of the FTS, the simulation calculates the resulting polarization angle, intensity, launch position, vector, and distance traveled. The parameters for the ray R are updated accordingly.

When interacting with an ellipsoid, an incident ray R_i is reflected as R_f and modified by inverting the component of its direction normal to the surface at the interaction point. This is represented as $\vec{v}_f = \vec{v}_i - 2(\vec{v}_i \cdot \hat{n})\hat{n}$, where $\hat{n}$ is the unit normal vector of the tangent plane, and both $\vec{v}_i$ and $\vec{v}_f$ are unit vectors. D_i is updated as $D_f = D_i + d(p_i, p_f)$, where $d(p_i, p_f)$ is the distance between the initial point of the incident ray p_i, and the reflection point of the ray off the ellipsoid at the point of intersection p_f. Since we are assuming ideal metal surfaces, the final polarization angle $\theta_f = \theta_i + \pi$, and the intensity is unchanged although a reflection coefficient could easily be added here.

At the wire-grid polarizers, an incident ray R_i has both reflected and transmitted parts parallel and orthogonal to the wire direction of the grid. A ray R_i with polarization angle θ interacting with a wire-grid polarizer at angle Φ, becomes two rays, one reflected R_{iR} and one transmitted R_{iT}:

$$R_i \equiv [\theta_i, I, p_i, \vec{v}_i, D_i], \tag{1a}$$

$$R_{iR} \equiv [\Phi, I \sin^2(\theta - \Phi), p_f, \vec{v}_f, D_i + d(p_i, p_f)], \tag{1b}$$

$$R_{iT} \equiv [\Phi + \pi/2, I \cos^2(\theta - \Phi), p_f, \vec{v}_i, D_i + d(p_i, p_f)]. \tag{1c}$$

The reflected ray is the light polarized such that $\theta = \Phi$, while the transmitted ray is polarized to $\theta = \Phi + \frac{\pi}{2}$. p_f is the intersection position of the incident ray with the polarizer, and $d(p_i, p_f)$ is the distance between the incident ray's initial launch point p_i and p_f. For the reflected ray, $\vec{v}_f$ is calculated by reflecting the incident unit direction vector $\vec{v}_i$ over the normal of the polarizer with the equation $\vec{v}_f = \vec{v}_i - 2(\vec{v}_i \cdot \hat{n})\hat{n}$, and the polarization is set to the angle of the polarizer. For the transmitted ray, the unit direction vector is unchanged, and the polarization is orthogonal to the polarizer. The magnitudes of the transmitted and reflected electrical fields are calculated with Eqs. (2a) and (2b), which is also shown in Fig. 3:

$$E_R = \sin(\theta - \Phi) E_0 \propto \sin(\theta - \Phi)\sqrt{I}, \tag{2a}$$

$$E_T = \cos(\theta - \Phi) E_0 \propto \cos(\theta - \Phi)\sqrt{I}, \tag{2b}$$

$$I \propto E_0^2 = |E_R|^2 + |E_T|^2. \tag{2c}$$

The radiation transfer is calculated by propagating rays in these manners through the FTS configuration. Upon reaching the detector, the parameters θ, I, and D are used to calculate the interference of all rays, as described in Section 3.C.

Each ray has 2^4 different paths through four polarizers. Half of these transfer paths end up at the second output port, just absorbed by a load in this simulation. The remaining eight paths reaching the detector are notated by R_{mk}, where m is the index for the n input light rays making up the simulated source ($m = 1 : n$), and k is the index for the eight light paths to the detector ($k = 1 : 8$).

Figure 4 shows the rays projected on the $x - y$ plane of two of the 16 possible paths. Solid lines are rays that are reflected by the first two polarizers (P1 and P2) and transmitted by the second two (P3 and P4), with corresponding colors to the path shown in Fig. 1 (solid lines). The black dashed line is a ray that is reflected

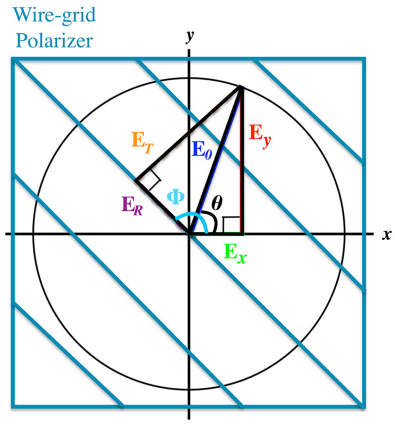


Fig. 3. Shown is a diagram of a light ray with intensity $I \propto E_0$ polarized at angle θ and the ray's projection onto the x and y axes. Light blue is a wire-grid polarizer at angle Φ. E_R and E_T are reflected and transmitted electric fields derived from Eqs. (2a) and (2b). E_x and E_y are the projections onto the two axes [Eqs. (4a) and (4b)].

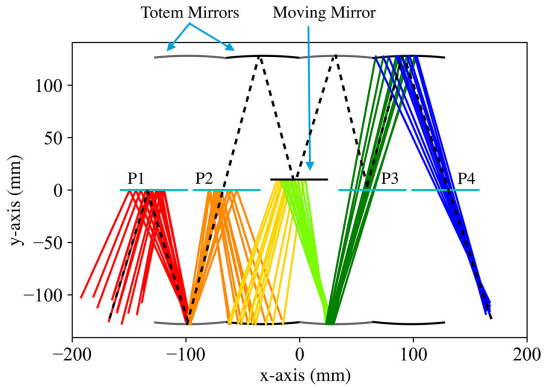


Fig. 4. Shown are 11 simulated rays projected onto the $x-y$ plane starting at the lower left where they intersect with the input mirror and ending on the lower right where they intersect with the output mirror. The totem mirrors are indicated by a curve where they intersect the $x-y$ plane. The blue lines along the x axis are the polarizers. The moving mirror is at the +10 mm position, lengthening the colored paths and shortening the path of one dashed ray shown transmitted by polarizer P2 (R_{dashed}). The beams are shown in the same colors as in Fig. 1 (or dashed black). The input and output mirrors are not shown. The ray bundle focus is displaced from the third totem and output mirrors because of the position of the moving mirror. At this mirror position, the nominal optical delay is +38.6 mm.

by the first and third polarizers (P1 and P3) but transmitted by the second and last polarizers (P2 and P4) (R_{dashed}). These are two interfering paths for one polarization, with the other not shown but interfering similarly. The moving mirror, shown by the solid black line at the center, is located at +10 mm from the origin.

Mirror movement along the y axis leads to a difference in path distance and a slight offset of the rays. In Fig. 4, as the mirror moves in the positive y direction, the distance traveled by R_{solid} increases, while the distance traveled by R_{dashed} decreases. The difference in path length creates a difference in the final phase when light rays along different paths are recombined, leading to interference patterns in the output interferogram.

C. Simulation of Power Detection

To calculate the detected power, we assume a single-mode detector and add the electric field of each ray R_{mk} and square it. This method simulates a single-mode detector with a flat phase front. We discuss the two steps in the two subsections below.

1. Electric Field of One Single Ray

Each ray is simulated independently, with interference occurring at the detector. The propagation of one ray, described below, applies to each ray traveling from the source-to-detector plane. One ray's $\vec{E}$ field at the detector with component amplitudes E_x and E_y and phase ϕ is of the form in Eq. (3):

$$\vec{E} = e^{i\omega t}[E_x e^{i\phi}\hat{x} + E_y e^{i\phi}\hat{y}]. \tag{3}$$

E_x and E_y are derived from $I \propto E_0^2$ and the polarization angle θ following Eqs. (4a) and (4b) as shown in Fig. 3:

$$E_x = E_0 \cos\theta \propto \sqrt{I}\cos\theta, \tag{4a}$$

$$E_y = E_0 \sin\theta \propto \sqrt{I}\sin\theta. \tag{4b}$$

An input ray R_m splits into eight paths, R_{mk} for $k = 1 \ldots 8$ and with n rays, $m = 1 \ldots n$. The distance a ray travels to the detector, D_k, is converted to phase, ϕ, for each wavelength, λ:

$$\phi_k = \frac{2\pi D_k}{\lambda}. \tag{5}$$

The electric field at the detector plane is calculated for each polarization. Rays falling off edges of optical elements or scattered are discarded. There are approximately eight times as many output rays as input rays, each with the following electric field at the detector:

$$E_x \mapsto E_{x,mk}e^{i\phi_{mk}}, \quad E_y \mapsto E_{y,mk}e^{i\phi_{mk}}.$$

2. Power from Many Rays

The nature of the simulation as a ray tracer means that rays represent discretized probability functions of a single photon from a source with a large emission beam and a finite limiting angle. The n initial rays R_i have identical initial phase and source point approximating a spherical phase wavefront, with launch vectors drawn from a distribution of vectors following the emitting beam pattern within the limited emission solid angle. The polarization of all rays is set along the $+x$ direction to match the experimental source. The approximation of power is calculated by summing all E_x and E_y of the $8,n$ simulated output Rays R_{mk} through the FTS box at the detector plane. The detected power is simulated by Eq. (6):

$$P_{\text{tot}} = \left(\sum_{k,m=1,1}^{8,n} E_{x,mk}\right)^2 + \left(\sum_{k,m=1,1}^{8,n} E_{y,mk}\right)^2. \tag{6}$$

The input source used in our experiment is a Gunn oscillator with either a waveguide antenna or a horn antenna, producing nearly spherical phase fronts at the input mirror. The simulation of this input is with rays with constant initial phase and a range of angles, which produces spherical phase fronts that match the experiment. In the receiving power simulation, we assume the receiver has a single-mode detector with zero phase error across the detecting area, which approximates feed horn-coupled single-mode detectors. The corrugated feed horns used widely in millimeter-wavelength astronomical observations are often designed with a small phase error in the aperture plane to prevent pattern degradation. The detected power in our simulation is then calculated by summing the electric field of all the rays R_{mk} within the detecting area with no additional phase added. This summation method, however, is not accurate for a multimode detector. The simulation mimics the effects of the compact nature of the FTS on the resolution, ray angle, source location, mirror displacement, as well as interference at the detector. However, the nature of the simulation as a ray tracer limits the ability to simulate power from electric fields because the ray tracer cannot model diffraction and does not consider scattering due to surface roughness. In addition, the power sum

in Eq. (6) works only for a single-mode detector. These limitations contribute to the differences between our measurements and simulation results, discussed later in Section 4.C.1.

3. Simulating the Detector

Our detector is a 4 K bolometer and is coupled to an amplifier with an output voltage approximately linear in the detected power. The detector has a finite thermal time constant, and the amplifier has an electric AC filter. The first step is the FTS calibration and requires determining these thermal and electronic transfer functions. We determine these by measuring the interferograms at different mirror scan speeds. The input is a blackbody source heated to 1300 K, and the detector is a multimode bolometer with a cold 25.4 mm thick piece of Fluorogole acting as a low-pass optical filter with a 1/2-power point at about 200 GHz [10]. The detector output is amplified and digitized while the mirror sweeps through a range of delay values. We model the detector output as the power interferogram filtered with a single pole at the detector time constant, τ, and an electronic zero at about 1 Hz. While the mirror position is read out absolutely, the delay position of the white light fringe is not known and varies over the course of several days. A further unknown initially is the resolution of the FTS. A broadband source such as a Planck thermal spectrum is likely to be highly resolved by the FTS, but a Gunn source is not. To take these unknowns together, we make a simplified model of an interferogram from a broadband source:

$$\psi_0 = a\frac{1}{\sqrt{2\pi}\,p}\cos(2\pi f(y-y_0))e^{\frac{-(y-y_0)^2}{2p^2}}, \tag{7}$$

where y_0 is the white light fringe position, f is the frequency of oscillation, p is the width of the interferogram, and a is amplitude. It is an approximation of the shape of an interferogram and captures the oscillation and decaying features of a broadband interferogram. Here the cosine function approximates the interference oscillation, and the Gaussian packet describes the decoherence of a broadband source. We use a Markov chain Monte Carlo (MCMC) [11] to fit the interferograms to Eq. (7) convolved with a single pole at time constant τ and find the five variables, a, f, p, y_0, and τ. This value of detector time constant τ is used to deconvolve the output of the physical FTS in subsequent runs. An example of this is shown in Fig. 5. In Fig. 5, the green line is the interferogram from a 30 mm/s optical scan with a blackbody source. The solid black line is the deconvolved interferogram using values returned by the MCMC, and the dashed blue line is an interferogram of the same source taken at a slower scan speed of 10 mm/s. A low-pass Fourier filter can remove the high-frequency noise in the deconvolved interferogram.

The time constant returned by the MCMC is 17 ms, so for low-frequency sources, it matters only if the velocity of the moving mirror is higher than approximately 20 mm/s. Slowing the speed of the mirror mitigates the distortion from the finite time constant, so subsequent runs were done at speeds around or below 10 mm/s to generate interferograms with minimal distortion by the impulse response, allowing direct comparison to the simulation.

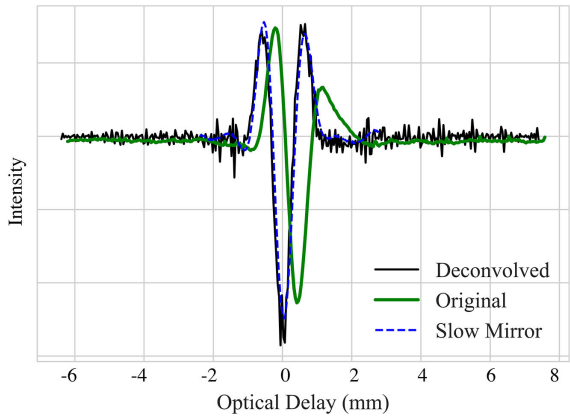


Fig. 5. Shown is a comparison of a broadband interferogram before and after deconvolution. The original interferogram (green) is from a blackbody source taken with an optical speed of 30 mm/s and is affected by the time constant of the detector. The interferogram taken at an optical speed of 10 mm/s (blue) is minimally affected by the time constant. The black interferogram is the green curve deconvolved with a time constant returned by the MCMC fit. It is closer to an interferogram without time decay, which should be symmetric. The amplified noise of the black curve is the result of deconvolving the low-pass electronic filter and does not affect the spectrum below 300 GHz.

4. SIMULATION OF THE FTS RESULTS

A. Beam Loss

Some light rays do not reach the detecting area because they are off the edges of the optical elements, especially at high optical delays. This effect can be quantified by tracing the fraction of rays that reach the detector as a function of the optical delay in the simulation, which generates a beam loss modulating envelope. This resulting modulating envelope shows the loss of rays due to the finite size of optical elements and is independent of source frequency. A simulated beam loss modulating envelope is shown in Fig. 6 and compared to a measured 90 GHz interferogram. 90 GHz, instead of a higher frequency, is used as a reference for less additional modulation from decoherence [12]. The black curve tapers at higher delays because more light rays are lost, and it does not contain information about the coherence level. This difference between the simulation and experiment is due to reduced interference at higher optical delays caused by decoherence, which is explained further in Section 4.B.

B. Decoherence

The two causes of decoherence discussed in this paper are what we call spatial decoherence and phase decoherence. In the FTS design shown in Fig. 1, spatial decoherence can dominate. In more classical systems with a mirror that travels along the light path, this effect is not present. For this system, a dominant nonideality comes when the intersection points for the light rays along different paths diverge on the detector plane as the moving mirror displaces along the y axis, as the light rays approach the center mirror at a small angle. This divergence is shown in Fig. 7, where the intersection points are plotted at different mirror displacements. The spatial divergence between the recombined

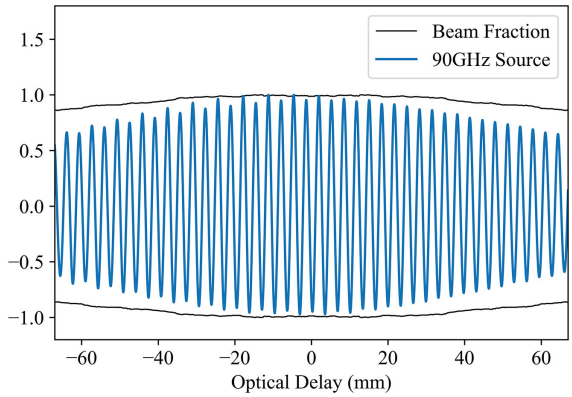


Fig. 6. Shown is the fraction of beams that reach the detector as a function of mirror position with a 90 GHz interferogram normalized to one for reference. The beam loss envelope decays slower than the modulating envelope of the measured interferogram at 90 GHz, which is from a combination of the beam loss and the decrease in coherence.

light rays leads to a decrease in spatial coherence and loss of signal at greater optical delays. Smaller diffraction (Airy) patterns at higher frequencies lead to smaller overlap of the diffraction patterns and greater loss of coherence level [12]. This effect results in narrower interferograms at higher frequencies. A narrower interferogram then returns a broader spectrum because the spectrum is a Fourier transform of the interferogram [13]. Therefore physical decoherence lowers resolution, especially at higher frequencies. The numerical simulation identified this effect as well. As discussed earlier, the ray-trace nature of the simulation limits its ability to simulate diffraction. Therefore, the spatial decoherence effect was not reflected in our power calculation and simulated interferograms. We can, however, quantify this effect approximately from the separation of the recombined locations and the overlap area of the Airy diffraction patterns.

Phase decoherence is caused by the wide beam angle in our instrument, which results in path length difference within the beam. In an FTS with large throughput and limited mirror size, the beams have a large solid angle at the beam splitters. The large solid angle leads to a non-uniform phase front for the recombined beams and a loss of coherence level. At a large enough optical delay, the phase of the beam center and the beam edge cancels the interference completely [14]. To maintain high throughput and interference level, the design of this instrument balances the phase decoherence effect with instrument size [4].

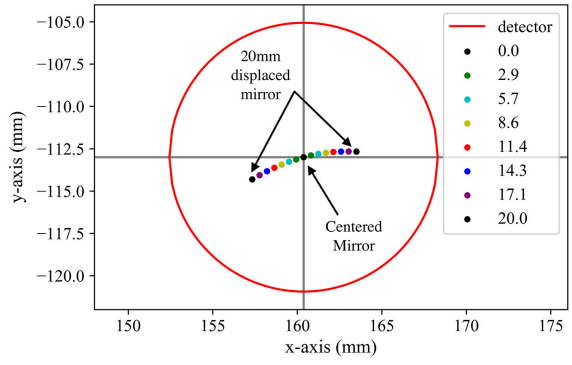


Fig. 7. Intersection points between the recombined light rays and the detector focal plane as the center mirror moves. The intersection points for different light paths from the same initial light ray are in the same color. When the moving mirror is at $y = 0$, the two intersection points from the interfering paths are at the center of the detector. As the moving mirror travels in the positive y direction, the intersection points of the different paths reflecting off different sides of the mirror become farther apart. This effect is an additional source of decoherence as the optical delay increases.

C. Comparison to Measurements

In the simulations, $n = 500$ light rays are launched from a single point source. Rays are emitted with a distribution uniform in azimuth and going as $\cos\theta$, where θ is the angle of the ray with the source plane normal and is constrained to hit the input mirror. Simulations include placing the point source at the center of the focal plane and several other off-center positions. From these simulated interferograms, we calculate the interference amplitude, power spectrum, and frequency resolution.

The simulations are compared to measured data. The source used in the experiment is a 144 GHz single-frequency Gunn oscillator coupled to the FTS through a waveguide antenna or a horn antenna. A two-axis motorized stage moves the source in a 20 mm × 20 mm area on the input focal plane. We use a monolithic silicon detector operated at 4.2 K as the detector. The experiment results are compared with the simulation results in the following sections. Averaging the resulting spectra weighted by their coupling approximates the effect of a narrowband extended source impinging on the FTS.

1. *Point Source at the Focal Plane Center*

Shown in Fig. 8 are the simulated and experimentally recorded interferograms from a source located at the center of the input focal plane. The data are filtered by a high-pass AC filter before fed into the analog-to-digital converter (ADC). The simulated interferogram is AC filtered similarly by setting the Fourier component of the apodized data below 1 Hz to zero and shifting the mean of the data to zero before inverse Fourier transforming into physical space. This returns the AC filtered and apodized simulated interferogram shown in Fig. 8(a). In comparison, the result of the experiment is shown in Fig. 8(b), which is apodized and AC filtered as well. The experimental interferogram falls off slower at higher optical delays than the simulation. The coherence length of the 144 GHz source is longer than the path through the instrument. We assume that the extended spectrum is due to scattering from imperfect mirror surfaces and other coherent reflections from metal surfaces other than the mirrors in the designed optical paths. This extra scattering and reflection is at the 10% level. Given the roughness level of 3.2 μm Ra, Ruze scattering from the mirrors is less than 1%. The additional coherent reflections from unintended surfaces can have two sources: 1) the absorptive materials do not fully cover the rims of the mirrors, which are likely to have reflections at high optical delays, and 2) the 10 mm thick open-cell polyurethane foam sheets used to cover the metal surfaces have a reflectivity of ∼3%. In comparison, the simulation assumes perfect reflection off mirrors and discards any rays that miss the mirrors. Note that the simulation does not include the diffraction effect and

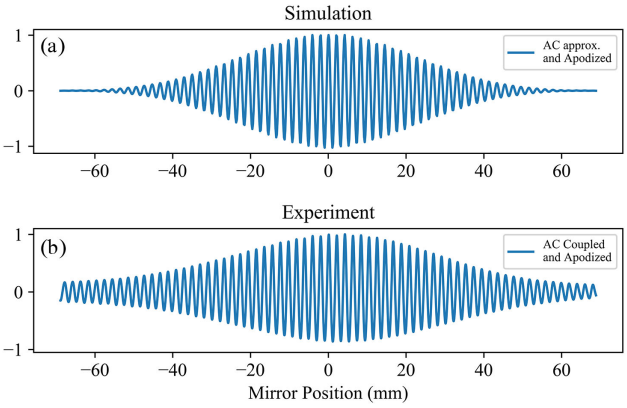


Fig. 8. Plotted are simulated and experimental interferograms. The simulated interferogram was generated with 500 rays to model a coherent 144 GHz source. The experimental interferogram was taken with the physical FTS, which is coupled to a 144 GHz centered source at the input and a monolithic silicon detector operated at 4.2 K at the output. Both interferograms are normalized to one. As discussed in Section C, this is due to the fact that the source is single mode and has a coherence length exceeding the instrument size.

therefore the spatial decoherence as well. Smoother mirrors and better absorption from all non-optical surfaces would reduce this effect. For any incoherent multimode source, this effect would vanish.

2. Shifted Source

The coupling efficiency and frequency resolution can vary as a function of the source location at the input focal plane. Moving the source within the input aperture can test the influence of the location of the source. For both simulation and experiment, the x and y coordinates of the source were shifted in 2.5 mm increments four times from the center in both directions, making up a 9×9 grid centered around [0,0]. The interference amplitudes of the 81 measurements are shown as a function of the grid position in Fig. 9, in which one pixel represents one interferogram. Both the simulation and experiment show less power coupling through the FTS as the source moves away from the center, with the simulation showing a faster decrease as the source is off-center. The extra power in the experiment with the source shifted is likely due to extra scattering and reflections described previously in Section 4.C.1.

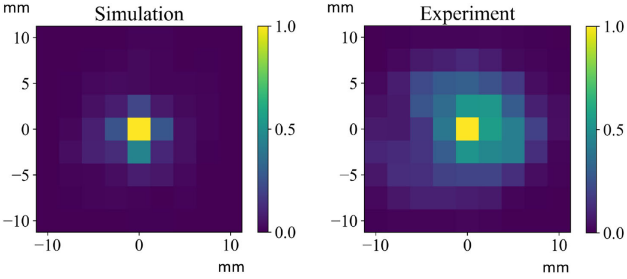


Fig. 9. Contour plots showing the amplitude of the interferograms at each of the 81 shifted source positions for the simulation (left) and the experiment (right). The amplitudes are normalized to one at the maximum when the source is at the center. The x and y axes represent the source's distance from the center.

3. Resolution of Source with a Finite Source

The physical sources used typically have a finite area. The summation of all 81 AC coupled, apodized, normalized interferograms can approximate the effect of a completely illuminated source plane. The resulting interferograms are shown in Figs. 10(a) and 10(b), with their Fourier transforms shown in Figs. 10(c) and 10(d). The full-width half-maximum (FWHM) of the spectrum was calculated by finding the width of the main peak at half-peak intensity. The shift of the spectra peaks seen in Figs. 10(c) and 10(d) show the effect of the solid angle of the compact FTS causing greater path lengths and introducing phase delay as compared to the central ray.

The resolution of an extended source at 144 GHz from adding all 81 interferograms is 7.1 GHz, which is different from the 4 GHz resolution reported in Ref. [4] previously due to an extra Hanning apodization window used in our analysis. In comparison, previous analysis [4] used a minimal cosine apodization window only at the edges of interferograms because the 295 GHz interferogram already tapers at high optical delays due to decoherence. In our analysis, the apodization is necessary because the simulation needs to be transformed into the Fourier domain and AC filtered before compared to the experiment. The resolution from adding all 81 simulated interferograms is 6.7 GHz, which is close to the experimental result. The small difference is caused by the limitations of the simulation, including the extra scattering and diffraction effects in the experiment not captured by the simulation. This simulation provides a method to predict the resolution of an FTS with a given geometry and will be useful for future FTS designs.

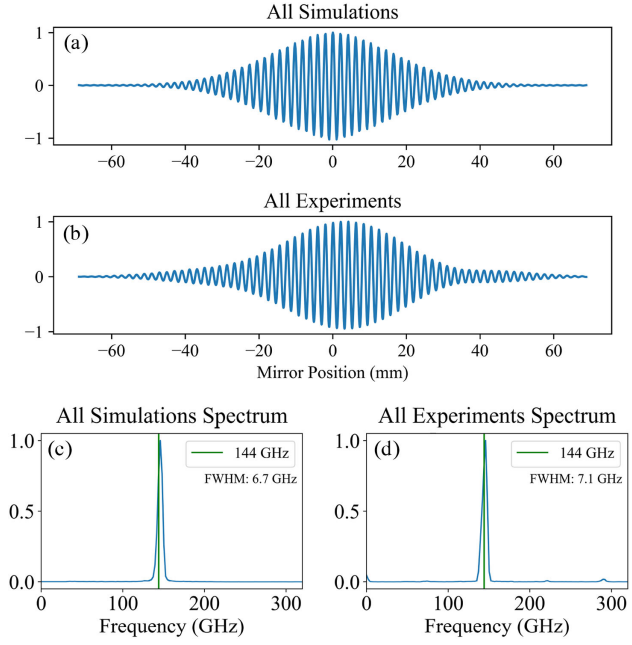


Fig. 10. Results of summing interferograms from all source locations, which can approximate sources with finite areas. The interferograms of all the positions are summed weighted by the intensity seen in Fig. 9. The spectra are Fourier transforms of the sum of all interferograms. The full-width half-maxima (FWHMs) of the main peaks of the spectra are the resolution.

5. CONCLUSION

This paper discusses a ray-trace-based numerical simulation of a compact FTS. The simulation tracks the properties of the light rays and generates interferograms using optical geometry and light ray propagation. We compare simulations of a single-mode source with a spherical phase wavefront detected by a single-mode detector to measurement. The actual measured resolution of 7.1 GHz was similar to the 6.7 GHz for the simulation, suggesting that we can evaluate the resolution, as well as other systematic effects of the geometry with this tool. Systematic effects that can be simulated are beam transfer loss, the decoherence at higher frequencies and higher optical delays, the finite physical size of the source, and shifted source location. Discrepancies between the simulated and experimental results point to non-negligible scattering, imperfect reflection on mirrors, and absorption on non-optical walls. The simulation can also be used to perturb individual alignments of the optics and optimize the operation with non-conic section mirrors. The simulation method can be extended to other FTS designs and can function as a tool to explore the FTS performance and geometry requirements.

Funding. National Science Foundation (DGE-1746045, PHY-1125897, PLR-1248097); Kavli Foundation; Gordon and Betty Moore Foundation (GBMF 947).

Disclosures. The authors declare no conflicts of interest.

REFERENCES

1. A. Kogut, D. T. Chuss, J. Dotson, D. J. Fixsen, M. Halpern, G. F. Hinshaw, S. Meyer, S. H. Moseley, E. J. W. M. D. Seiffert, and D. N. Spergel, "The primordial inflation explorer (pixie)," Proc. SPIE **8146**, 81460T (2011).
2. Z. Pan, P. A. R. Ade, Z. Ahmed, A. J. Anderson, J. E. Austermann, J. S. Avva, R. B. Thakur, A. N. Bender, B. A. Benson, J. E. Carlstrom, F. W. Carter, T. Cecil, C. L. Chang, J. F. Cliche, A. Cukierman, E. V. Denison, T. de Haan, J. Ding, M. A. Dobbs, D. Dutcher, W. Everett, A. Foster, R. N. Gannon, A. Gilbert, J. C. Groh, N. W. Halverson, A. H. Harke-Hosemann, N. L. Harrington, J. W. Henning, G. C. Hilton, W. L. Holzapfel, N. Huang, K. D. Irwin, O. B. Jeong, M. Jonas, T. Khaire, A. M. Kofman, M. Korman, D. Kubik, S. Kuhlmann, C. L. Kuo, A. T. Lee, A. E. Lowitz, S. S. Meyer, D. Michalik, J. Montgomery, A. Nadolski, T. Natoli, H. Nguyen, G. I. Noble, V. Novosad, S. Padin, J. Pearson, C. M. Posada, A. Rahlin, J. E. Ruhl, L. J. Saunders, J. T. Sayre, I. Shirley, and E. Shirokoff, "Optical characterization of the SPT-3G camera," J. Low Temp. Phys. **193**, 305–313 (2018).
3. B. A. Benson, P. A. R. Ade, Z. Ahmed, S. W. Allen, K. Arnold, J. E. Austermann, A. N. Bender, L. E. Bleem, J. E. Carlstrom, C. L. Chang, H. M. Cho, J. F. Cliche, T. M. Crawford, A. Cukierman, T. de Haan, M. A. Dobbs, D. Dutcher, W. Everett, A. Gilbert, N. W. Halverson, D. Hanson, N. L. Harrington, K. Hattori, J. W. Henning, G. C. Hilton, G. P. Holder, W. L. Holzapfel, K. D. Irwin, R. Keisler, L. Knox, D. Kubik, C. L. Kuo, A. T. Lee, E. M. Leitch, D. Li, M. McDonald, S. S. Meyer, J. Montgomery, M. Myers, T. Natoli, H. Nguyen, V. Novosad, S. Padin, Z. Pan, J. Pearson, C. Reichardt, J. E. Ruhl, B. R. Saliwanchik, G. Simard, G. Smecher, J. T. Sayre, E. Shirokoff, A. A. Stark, K. Story, A. Suzuki, K. L. Thompson, C. Tucker, K. Vanderlinde, J. D. Vieira, A. Vikhlinin, G. Wang, V. Yefremenko, and K. W. Yoon, "SPT-3G: a next-generation cosmic microwave background polarization experiment on the south pole telescope," Proc. SPIE **9153**, 91531P (2014).
4. Z. Pan, M. Liu, R. Basu Thakur, B. A. Benson, D. J. Fixsen, H. Goksu, E. Rath, and S. Meyer, "Compact millimeter-wavelength Fourier-transform spectrometer," Appl. Opt. **58**, 6257–6267 (2019).
5. R. B. Thakur, H. Goksu, M. Liu-Sarkar, R. Mbarek, Z. Pan, S. Meyer, and B. Benson, "Compact Fourier transform spectrometer," in *CMB-S4 Workshop*, Harvard University, Boston, Massachusetts, USA, August 24–25, 2017.
6. L. Mach, "Ueber einen interferenzrefraktor," Z. Instrum. **12**, 806 (1892).
7. L. Zehnder, "Ein neuer interferenzrefraktor," Z. Instrum. **11**, 275 (1891).
8. D. A. Naylor, B. G. Gom, I. Schofield, G. Tompkins, and G. R. Davis, "Mach-Zehnder Fourier transform spectrometer for astronomical spectroscopy at submillimeter wavelengths," Proc. SPIE **4855**, 540–551 (2003).
9. P. Hariharan, *Optical Interferometry* (Elsevier, 2003).
10. M. Halpern, H. Gush, E. Wishnow, and V. D. Cosmo, "Far-infrared transmission of some dielectrics at cryogenic and room temperatures: Fluorogold, Ecosorb, Stycast, and various other plastics," Appl. Opt. **25**, 565–570 (1986).
11. D. Foreman-Mackey, D. W. Hogg, D. Lang, and J. Goodman, "EMCEE: the MCMC hammer," Publ. Astron. Soc. Pac. **125**, 306–312 (2013).
12. J. E. Greivenkamp, *Field Guide to Geometrical Optics* (SPIE, 2004), Chap. 88.
13. E. Brigham, *The Fast Fourier Transform and Its Applications* (Prentice-Hall, 1988), Chap. 3.
14. J. Chamberlain, *The Principles of Interferometric Spectroscopy* (Wiley-Interscience, 1979), Chap. 6.

205.208.121.179 {ts '2020-09-08 11:37:08'}